

pubs.acs.org/acsapm Article

Low-Density, Semicrystalline Poly(phenylene sulfide) Aerogels Fabricated Using a Benign Solvent

Garrett F. Godshall, Glenn A. Spiering, Erin R. Crater, and Robert B. Moore*



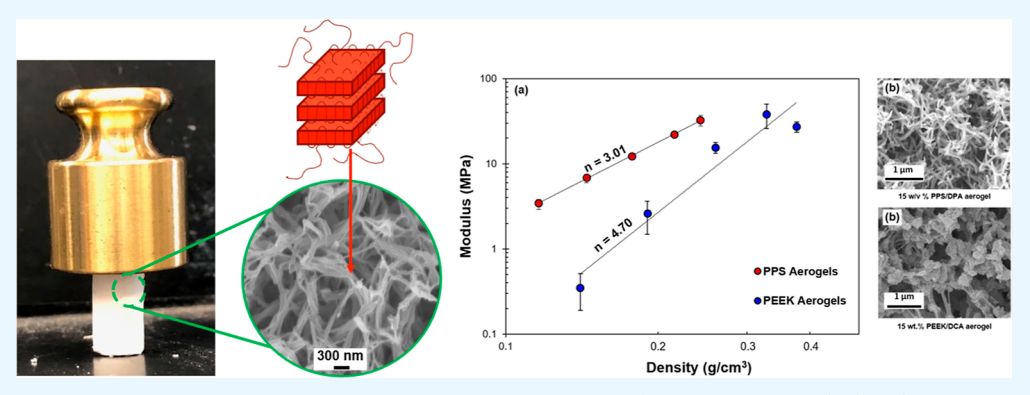


ACCESS

Metrics & More

Article Recommendations

Supporting Information



ABSTRACT: Utilizing a thermally induced phase separation process, poly(phenylene sulfide) (PPS) thermoreversible gels are developed using for the first time a benign solvent, 1,3-diphenylacetone (DPA). The PPS/DPA phase diagram revealed a solidliquid phase separation mechanism often observed with crystallizable polymers in good solvents. Two different methods of determining the Flory-Huggins interaction parameter, χ , were utilized to understand the polymer-solvent interactions that govern the phase behavior. Using an experimental approach, a melting point depression curve was fit to experimental PPS/DPA melting point data, revealing an interaction parameter of $\chi = 0.41$. Using accepted Hansen solubility parameters of PPS and calculated parameters for DPA via a group contribution method, the polymer–solvent interaction parameter was estimated to be $\chi = 0.49$. The reasonable agreement between both methods indicates good interactions between PPS and DPA and verifies the calculated solubility parameters for DPA. Upon gelation at temperatures below 225 °C, subsequent solvent evacuation via freeze-drying yields aerogels with low densities ranging from 0.11 to 0.25 g/cm³ and volumetric porosities ranging from 92.3 to 82.2%. The physical properties of the PPS aerogels were found to be comparable to similar aerogels made from poly(ether ether ketone) (PEEK). Ultra-small to wideangle X-ray scattering (USAXS/SAXS/WAXS) profiles reveal an ordered, hierarchical morphology with sharp interfaces, whereby the microstructure is composed of semicrystalline aggregates of stacked lamella. Scanning electron microscopy micrographs indicate that the PPS aerogels are highly porous and that the lamellar stacks take the form of elongated, interconnected fibrils. Power-law scaling of aerogel density with compressive modulus suggests a tendency of the interconnected lamellar aggregates to bend and/or buckle in compression in a manner similar to strut deformation in open-celled foams. Despite their similar physical properties, PPS aerogels demonstrated higher moduli than PEEK aerogels at comparable densities due to their network-like morphology.

KEYWORDS: aerogels, mechanically robust, low-density, polyphenylene sulfide, phase diagram, hierarchical porosity, Hansen solubility parameters

INTRODUCTION

Aerogels are dry, solid materials with high degrees of porosity, low densities, and low thermal conductivities. Aerogels were first invented in 1931 by Kistler, and since their inception, much study has been dedicated to their fabrication, characterization, and application. Polymeric aerogels are of particular interest due to their enhanced flexibility compared to inorganic aerogels. Polymeric aerogels are created by the evacuation of the solvent from a swollen multiphase polymeric network, leaving behind a porous framework. These aerogel networks can be constructed of covalent crosslinks, polymer crystallites, chain entanglements,

hydrogen bonds, ionic aggregates, particulate agglomerates, or a combination of multiple types of crosslinks.^{4–8}

Physical aerogels are one subsection of polymeric aerogels which differ from covalent aerogels in that their network

Received: June 11, 2023 Accepted: August 28, 2023



connectivity is derived from non-permanent and often thermally labile junctions, which constitute a physically crosslinked network. Several semicrystalline polymers that are devoid of hydrogen-bonding groups or ionic functionalities have been shown to form aerogels, with polymer crystallites and chain entanglements acting as the physical crosslinks within the open microstructure. Part Recent examples of crystallizable polymers that have been shown to form physical aerogels include syndiotactic polystyrene, isotactic polypropylene, poly(phenylene oxide), poly(vinylidene fluoride), poly(L-lactide) and poly(L-lactide)/poly(D-lactide) blends, and poly(ether ether ketone). Current applications of physical polymeric aerogels include three-dimensional separation membranes, airborne nanoparticle filters, catalysis supports, thermal insulation, and gel-state platforms for blocky copolymer functionalization. Expanding the applicability of physical aerogels necessitates the transition to high-performance polymers.

Poly(phenylene sulfide) (PPS) is a high-modulus, semicrystalline engineering thermoplastic with a high melting point $(T_{\rm m} = 285 \, ^{\circ}\text{C})$ and a relatively low glass transition temperature $(T_g = 90 \, ^{\circ}\text{C})$, making PPS more melt-processable compared to similar materials.²⁴ Bulk PPS is stiff but fairly brittle (Young's modulus, E = 3.6 GPa; elongation at break, $\varepsilon_{\text{break}} = 1-2\%$) relative to more ductile poly(ether ether ketone) (PEEK) (E =3.6 GPa, $\varepsilon_{\text{break}}$ = 50%) and poly(ethylene terephthalate) (PET) $(E = 3 \text{ GPa}, \varepsilon_{\text{break}} = 50-300\%).^{25} \text{ Additionally, PPS displays}$ good thermal and chemical stabilities, rendering it applicable in various automotive, electrical, aerospace, adhesive, and coatings industries where high temperatures and harsh chemical environments are expected. ^{24,26} To date, only a small number of strong acids and high-boiling-point solvents are known to dissolve PPS, and often dissolution must take place at high temperatures. Interestingly, once dissolved and subsequently cooled, certain PPS-solvent systems can form microphaseseparated structures. Some of the applicable solvents include diphenyl ketone, $^{27-30}$ diphenyl sulfone, 31,32 diphenyl isophthalate, 32 benzoin, 30,32 ε -caprolactam, 32 hydrogenated terphenyl, 32 and cyclohexylpyrrolodinone. 32 Once dissolved and then cooled, the resulting microphase-separated structures are the solvated precursors to highly porous physical polymeric aerogels.

Thin, porous separation membranes and three-dimensional polymeric physical aerogels have been fabricated from a variety of polymers via thermally induced phase separation (TIPS) processes. 15-17,20,33-36 In these processes, a homogeneous polymer solution is formed at a high dissolution temperature. As the solution cools through an upper critical solution temperature (UCST) phase boundary, phase separation is induced. 37 When polymer-solvent interactions are unfavorable, a heterogeneous morphology can develop by liquid-liquid (L-L) phase separation, forming bicontinuous or cellular morphologies.³⁷ At high polymer concentrations or when polymer-solvent interactions are strong, solid-liquid (S-L) phase separation occurs and axialitic or spherulitic morphologies are formed.³⁸ Evacuation of the gelation solvent, either via supercritical CO₂ extraction, lyophilization, or the exchange with and evaporation of a low boiling point solvent, creates the highly porous polymeric aerogel framework. Based on the phase separation mechanism, thin PPS TIPS membranes have been shown to form bicontinuous, cellular, axialitic, and spherulitic morphologies.^{27–32,39} However, to date, no work has been reported on

the morphological and mechanical properties of these threedimensional PPS aerogels manufactured from the TIPS process.

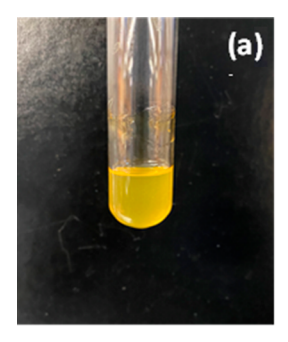
In this report, the fabrication of PPS thermoreversible gels using a benign FDA-approved food additive, 40 1,3-diphenyl acetone (DPA), as the gelation solvent is detailed. To our knowledge, this is the first known report of using DPA as a gelation solvent for PPS. While previous research has been devoted to creating thin, porous PPS membranes via TIPS from a variety of more hazardous solvents, this work investigates the nature of three-dimensional PPS aerogels as structurally robust monoliths. The purpose of this study is to elucidate the phase behavior of PPS and DPA through the construction of a temperature-composition phase diagram and the calculation of the Flory-Huggins interaction parameter through two distinct methods. Furthermore, the effect of polymer composition on the microstructure and mechanical behavior of PPS aerogels is explored. Local and global aerogel morphologies were analyzed via complementary microscopy and scattering techniques, and relationships between physical properties and mechanical behavior are discussed.

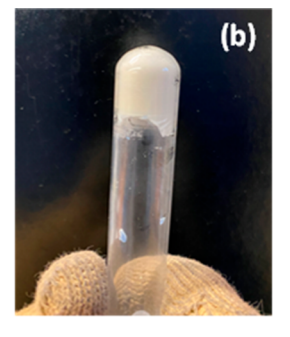
■ EXPERIMENTAL METHODS

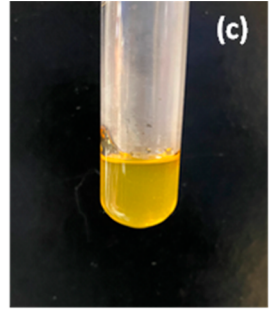
Materials. PPS (Ryton QA200N) was provided by Solvay Specialty Polymers (Alpharetta, GA). DPA (99.0%) was purchased from J&K Scientific (Beijing, China) and Oakwood Chemical (Estill, SC). Ethanol (200 proof, 100%, USP, Decon Labs) was purchased from Fisher Scientific Company. All polymers and chemicals were used as received. Open-ended glass test tubes, with a nominal internal diameter of 7.5 mm and a length of 60 mm, were cut in-house. Aluminum test tube blocks were purchased from Research Products International (Mount Prospect, IL).

Aerogel Preparation. PPS granules were pre-mixed with solid DPA ($T_{\rm m} = 32-34$ °C⁴¹) in a round-bottom flask at various weight-tovolume ratios (10, 15, 20, 25, and 30 w/v%) and then heated to 270 °C in a metal bath with constant stirring until dissolved. Complete dissolution occurred between 10 and 20 min, depending on the concentration. The solutions were then immediately poured into openended hollow glass tubes, which were resting in an aluminum test tube block at ambient temperature. The hot solutions completely solidified in roughly 1-3 min at temperatures below 225 °C. Due to rapid gelation, there was a negligible amount of polymer solution which leached from the hollow tube into the aluminum block. Once the gels were solidified and cooled, they were immediately removed from the aluminum block and placed in an ethanol bath to solvent exchange the DPA with ethanol. During the solvent exchange process, the ethanol bath was maintained at a temperature of 50 °C to prevent any DPA from crystallizing, which might have altered the gel morphology. After 24 h, the solvated organogels were pushed through open-ended glass tubes and returned to a fresh ethanol bath. The ethanol was refreshed twice a day for 4 days to completely replace the DPA with ethanol. The ethanol-exchanged organogels were then transferred to a roomtemperature water bath for a period of 4 days, cycling in fresh water once a day to completely replace the ethanol with water, creating hydrogels. Cylindrical hydrogels were then cut to length, frozen overnight at -18 °C, and then lyophilized (LabConco) to create PPS aerogels.

Aerogel Characterization. Cloud point measurements were performed on a Nikon Eclipse LV100 optical microscope equipped with a Linkam HFSX350-CAP hot stage outfitted with a 1.7 mm diameter capillary port. The turbidity of PPS solutions was monitored using an AmScope MU503B digital CMOS camera and AmScope software. Solidified, solvated gels were ground into a fine powder and packed into 1.5 mm diameter Pyrex capillaries, which were subsequently flame-sealed with a torch. To determine the cloud point, capillaries were heated in the hot stage to 320 °C at 50 °C/min, held isothermally for 3 min, and cooled at 10 °C/min to 40 °C. Snapshots of the capillary were taken (one per second), and the







(b)

(One Phase)

Crystallization

spinodal

0.75

0.5

Figure 1. Confirmation of thermoreversibility of the PPS/DPA system: (a) PPS/DPA solution at 270 °C; (b) PPS/DPA organogel after cooling to room temperature; and (c) re-dissolution of the gel at 270 °C.

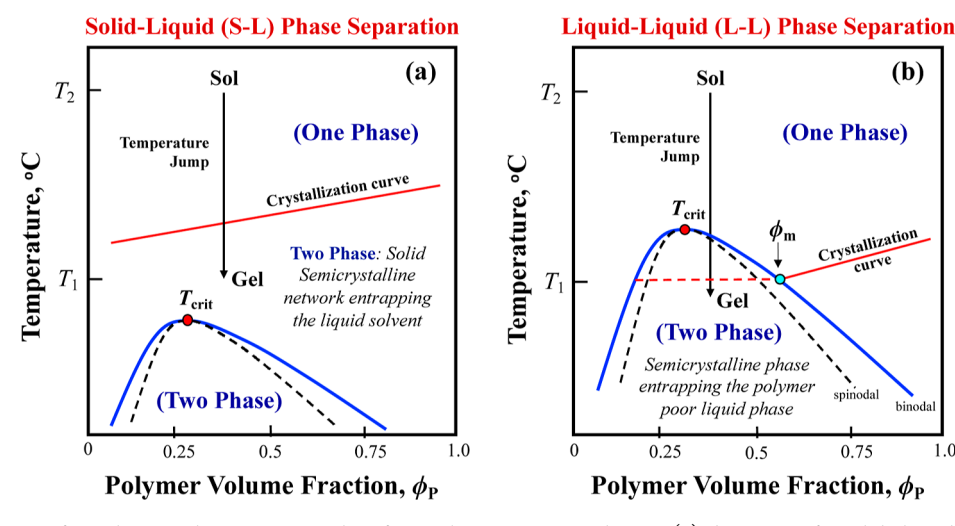


Figure 2. Phase diagrams for polymer gelation upon cooling from a homogeneous solution; (a) depiction of a solid-liquid (S-L) phase diagram involving direct crystallization from solution, and (b) a liquid—liquid (L-L) phase diagram where crystallization occurs within a resulting polymer-rich phase. T_{crit} is the UCST.

brightness of each image was extracted using the ImageJ image analysis software. A plot of brightness versus temperature was constructed (see Figure S1), and the cloud point temperature was taken as the onset of brightness decrease using TRIOS data analysis software. Three replicate samples were tested for each polymer/solvent composition.

Differential scanning calorimetry (DSC) experiments of the solvated gels to complete the phase diagram were completed using a TA Instruments Q2000 DSC using the following experimental protocol: three replicate samples of each polymer/solvent composition were first sealed in hermetic pans. The samples were then heated at 10 °C/min to 320 °C, held isothermally at 320 °C for 3 min to fully dissolve the PPS, cooled at 10 $^{\circ}\text{C/min}$ to 40 $^{\circ}\text{C}$, and then once again heated to 320 $^{\circ}\text{C}$ at 10 °C/min. The melting temperature (T_m) was taken as the peak of the melting endotherm during heating scans, and the crystallization temperature (T_c) was taken as the minimum of the crystallization exotherm during cooling scans. The onset of crystallization $(T_{c,onset})$ was taken as the onset of slope change from the baseline to the exotherm during the cooling scan.

Aerogel morphology was analyzed using a LEO (Zeiss) 1550 fieldemission scanning electron microscopy (FE-SEM) with in-lens detection. Aerogel samples were sputter-coated with a 5 nm-thick layer of iridium using a Leica EM ACE600 sputter coater. The data analysis software ImageI was used to collect dimensional data on the microstructure of PPS aerogels. At least 50 features were measured in each analysis. Ultra-small-angle X-ray scattering (USAXS), small-angle X-ray scattering (SAXS), and dynamic wide-angle X-ray scattering (WAXS) experiments utilizing a Linkam HFSX350-CAP hot stage were conducted at beamline 9-ID-C at the Advanced Photon Source (APS) at Argonne National Labs (Lemont, IL). 42,43 For contrast-matching experiments, a 20 w/v % PPS aerogel was submerged in excess ethanol/ Cyrene mixtures for 96 h prior to data collection. The Nika macro for

Igor Pro was utilized to develop SAXS and WAXS data,⁴⁴ and the Irena macro for Igor Pro was used to reduce USAXS data and merge USAXS/ SAXS profiles. 45 Wide-angle X-ray diffraction (WAXD) experiments of PPS aerogels were performed on a Xenocs Xeuss 3.0 SAXS/WAXS equipped with a GeniX 3D Cu HFVLF microfocus X-ray source utilizing Cu K α radiation (λ = 0.154 nm). The sample-to-detector distance was 43 mm, and the q-range was calibrated using a lanthanum hexaboride standard. Measurements were collected at room temperature using 30 min exposure times on a Dectris EIGER 4 M detector. Data reduction was performed using XSACT software provided by Xenocs. The fractional degree of crystallinity, X_{c} , of the PPS aerogels and melt-crystallized PPS film was calculated as

$$X_{c} = \frac{\int_{0}^{\infty} q^{2} I_{c}(q) \, dq}{\int_{0}^{\infty} q^{2} I(q) \, dq}$$
 (1)

where q equals the scattering vector and $I_c(q)$ and I(q) represent the scattering intensity of the crystalline reflections and the total scattering intensity, respectively. The amorphous profile of PPS was scaled according to the method of Vonk.

Uniaxial compression tests were executed using an Instron 4204 testing machine retrofitted with an MTS ReNew upgrade package and affixed with 50 mm compressive platens. Tests were run using a 5 kN load cell and a 1 mm/min crosshead speed. Cylindrical aerogel sample dimensions were 15 mm in length by 7.5 mm in diameter, in accordance with the 2:1 length-to-diameter ratio required by ASTM D695-15. Three aerogel samples of each composition for compression testing, density measurements, and porosity measurements were run. Porosity was calculated according to ASTM D6226-15 using a Micromeritics AccuPyc 1340 gas pycnometer equipped with a 1 cm³ insert and a

helium equilibration rate of 0.03 psig/min. The porosity, P, was determined from the skeletal density, $V_{\rm spec}$, reported from the pycnometer as

$$P = \left[\frac{(V - V_{\text{spec}})}{V} \right] \times 100 \tag{2}$$

where $V = \pi r^2 l$, the geometric volume of the porous cylindrical specimen, r is the cylinder radius, and l is the cylinder length. Table S1 highlights the density, porosity, and compressive modulus of each aerogel composition.

RESULTS AND DISCUSSION

PPS is known for its high chemical stability compared to other common crystallizable thermoplastics. Significant PPS dissolution has only been reported in a select group of high-boiling heterocyclic aromatic hydrocarbon solvents at temperatures close to the melting point of the polymer. 47 The list of industrially viable solvents becomes quite limited when cost and environmental considerations are made. Additionally, some acids, such as sulfuric acid and oleum, have been shown to dissolve PPS; however, these systems are also used in sulfonation reactions of the polymer and may in fact react with the system rather than purely dissolve the compound.⁴⁷ In our search for a new, benign solvent for PPS, we have found that DPA ($T_b = 330$ °C) is able to completely dissolve PPS in a matter of minutes. Upon cooling the PPS/DPA solution, a thermoreversible gel is formed, whereby the physical crosslinks are thermally labile upon melting and re-formable via polymer crystallization upon cooling.8 Figure 1 demonstrates the thermoreversibility of a 15 w/v % PPS-DPA system.

In the TIPS process, it is generally observed that crystallizable polymers dissolved in a good solvent phase-separate upon cooling from T_2 to T_1 via a solid-liquid (S-L) mechanism (Figure 2a), where crystallization occurs at temperatures below a compositionally dependent melting temperature (see eq 3 below). 37,38 In contrast, crystallizable polymers dissolved in a poor solvent often undergo liquid-liquid (L-L) phase separation upon cooling from T_2 to T_1 (Figure 2b), where a thermodynamically unstable solution first decomposes into a polymer-poor liquid phase and a polymer-rich liquid phase. 37 As the system is progressively cooled, the polymer volume fraction in the polymer-rich phase increases until it reaches the monotectic composition (i.e., ϕ_{m} at the intersection of the crystallization curve and the binodal phase boundary).48 Subsequently, at this monotectic temperature and composition, crystallization within the polymer-rich phase occurs.

Based on the phase behavior depicted in Figure 2, a characteristic distinction between the S-L and L-L phase separation processes is linked to the compositional dependence of the crystallization temperature, T_{c} , and cloud-point temperature, $T_{\rm cloud}$. For the S-L process, $T_{\rm c}$, and $T_{\rm cloud}$ are both generally dependent on the polymer volume fraction, $\phi_{\rm P}$. In this direct crystallization from solution process, melting point depression (and concurrent T_c depression of the supercooled solution) is dependent on the polymer/solvent composition and attributed to a reduced chemical potential of the polymer/ solvent mixture compared to that of the pure polymer [e.g., as depicted by the sloped crystallization curve, Figure 2a. 49 Upon cooling to a temperature below the crystallization curve (e.g., T_1), crystal nucleation initiates the growth of large lamellar aggregates. Once the size of the crystalline aggregates becomes comparable to the wavelength of visible light, light scattering is observed, resulting in a turbid suspension. Consequently, in the

S–L process, both $T_{\rm c}$ and $T_{\rm cloud}$ are compositionally dependent such that the crystallization temperature coincides with the observation of turbidity (i.e., following the same compositional dependence).

In contrast, for the L-L process, the T_c is generally independent of composition upon cooling to the monotectic temperature on the UCST phase boundary (assuming L-L phase separation precedes crystallization).⁴⁸ For example, upon cooling toward T_1 , below the UCST, two different initial compositions (e.g., $\phi_{\rm P}$ = 0.25 and $\phi_{\rm P}$ = 0.5) will both phaseseparate into the same two compositions of coexisting polymerpoor and polymer-rich phases set along the binodal boundary (Figure 2b). Once the temperature reaches the monotectic temperature, crystallization will occur at ϕ_{m} within the polymerrich phase. Thus, T_c is constant within the binodal phase boundary (i.e., the dashed crystallization line at T_1 in Figure 2b). With respect to the cloud point during this L-L phase separation process, turbidity is attributed to light scattering resulting from a significant contrast in the refractive indices of the two coexisting liquid phases. Consequently, the cloud point, $T_{\rm cloud}$, is expected to follow the parabolic compositional dependence of the UCST phase boundary.³⁷ Therefore, in the L–L process, for compositions less than $\phi_{
m m}$, only the $T_{
m cloud}$ is compositionally dependent, having no coincidence with T_c .

To understand the phase separation mechanism as a means to control morphological development within gels formed via a TIPS process, a phase diagram must be constructed. The phase diagram in Figure 3 shows the onset temperatures of

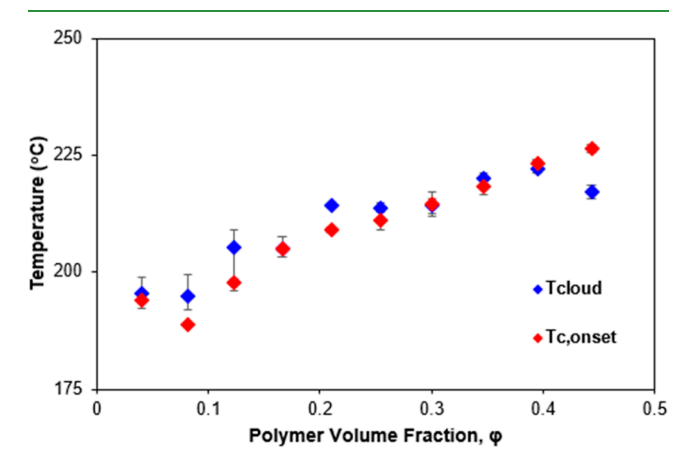


Figure 3. Onset temperature of crystallization and cloud point temperature versus polymer composition phase diagram for the PPS/DPA system.

crystallization, $T_{\rm c,onset}$ and the cloud points, $T_{\rm cloud}$, versus the composition of the PPS/DPA system over a wide range of PPS concentrations. From these data, it is clear that $T_{\rm c,onset}$, upon cooling from $T=300\,^{\circ}{\rm C}$, shows a strong dependence on polymer concentration. Additionally, the cloud point temperature follows the same compositional dependence as that of the $T_{\rm c,onset}$ curve, with very close agreement between $T_{\rm c,onset}$ and $T_{\rm cloud}$. Thus, as described above, this compositionally dependent behavior is characteristic of a solid–liquid (S–L) phase separation system, where polymer crystallizes from the concentrated solution without liquid–liquid (L–L) phase separation occurring. ³⁸

In order to rationalize the observed S–L phase separation behavior in a TIPS system (characteristic of polymers in good solvents), the Flory–Huggins interaction parameter, χ , is often

calculated to quantify the polymer–solvent interactions. This unitless value indicates the quality of the solvent as it relates to polymer miscibility or immiscibility in a given solvent. Theoretically, $\chi=0.5$ indicates theta conditions⁵⁰ (i.e., polymer–polymer interactions are comparable to the polymer–solvent interactions). In general, $\chi<0.5$ indicates a good solvent, while $\chi\gg0.5$ indicates a poor solvent.^{37,38}

The Flory–Huggins interaction parameter may be calculated using solubility parameters, which are measures of the cohesive energy density of a given material. Generally, the closer the solubility parameters of two entities in a mixture are, the more favorable the interactions between the constituents. In particular, the Hansen solubility parameters (HSPs) quantify the individual attributes of the dispersive, polar, and hydrogenbonding interactions of a given compound, generally yielding a more accurate estimation of overall solubility. Thus, determination of χ using HSPs of the polymer and solvent is done as follows 51

$$\chi = \chi_{H} + \chi_{S}$$

$$= \frac{V_{\text{solv}}}{RT} \left[\left(\delta_{\text{poly}}^{D} - \delta_{\text{solv}}^{D} \right)^{2} + (0.25) \left(\delta_{\text{poly}}^{P} - \delta_{\text{solv}}^{P} \right)^{2} + (0.25) \left(\delta_{\text{poly}}^{HB} - \delta_{\text{solv}}^{HB} \right)^{2} \right] + \chi_{S} \tag{3}$$

where δ_i^D , δ_i^P , and δ_i^{HB} refer to the dispersive, polar, and hydrogen-bonding partial solubility parameters of the polymer or solvent, respectively, 52 χ_H is the enthalpic contribution to χ , and χ_S is the entropic contribution to χ , generally accepted as $\chi_S = 0.34$ for polymer solutions. 53 The experimentally determined HSP values for PPS are $\delta_{PPS}^D = 18.7$, $\delta_{PPS}^P = 5.3$, and $\delta_{PPS}^H = 3.7$ MPa $^{1/2,51}$ The HSPs for DPA could not be found in the literature; therefore, they were calculated using the group contribution method by Stefanis and Panayiotou. 54 The details of these calculations for the HSP of DPA can be found in the Supporting Information.

Using the HSP values reported for PPS⁵¹ and the calculated HSP values for DPA, χ was calculated to be 0.49, using eq 3. For comparison, the same group contribution method was used to calculate the HSPs for 4-benzoylbiphenyl, a solvent used in another PPS TIPS system which undergoes S–L phase separation. The interaction parameter for this system was found to be 1.26. These calculations can be found in the Supporting Information.

An empirical method of calculating χ involves the use of Flory's melting point depression equation, ⁵⁶ which expresses the melting temperature depression of a semicrystalline polymer in the presence of a solvent at a specific solvent volume fraction, ϕ_s

$$\frac{1}{T_{\rm m}} - \frac{1}{T_{\rm m}^{\rm o}} = \frac{RV_{\rm p}}{\Delta H_{\rm f}^{\rm o} V_{\rm s}} (\phi_{\rm s} - \chi \phi_{\rm s}^2) \tag{4}$$

where $T_{\rm m}$ is the experimental melting temperature of the semicrystalline polymer/solvent system, $T_{\rm m}^{\rm o}$ is the equilibrium melting temperature of PPS ($T_{\rm m}^{\rm o}=308\,^{\circ}{\rm C}^{\rm S7}$), R is the universal gas constant, $V_{\rm p}$ is the molar volume of the polymer repeat unit ($V_{\rm p}=81.3\,{\rm cm^3/mol}$), $V_{\rm s}$ is the molar volume of the solvent ($V_{\rm s}=196.7\,{\rm cm^3/mol}$), $\Delta H_{\rm f}^{\rm o}$ is the enthalpy of fusion per mol of repeat units for an infinitely thick PPS crystal ($\Delta H_{\rm f}^{\rm o}=8.65\,{\rm kJ/mol^{S8}}$), and χ is the Flory–Huggins interaction parameter. This equation can be reorganized to solve for the experimentally measurable $T_{\rm m}$

$$T_{\rm m} = \frac{1}{\frac{RV_{\rm p}(\phi_{\rm s} - \chi\phi_{\rm s}^2)}{\Delta H_{\rm f}^{\rm o}V_{\rm s}} + \frac{1}{T_{\rm m}^{\rm o}}}$$
(5)

Thus, fitting experimental melting point data to the curve generated via eq 5 using a sum of squares technique yields an estimation of γ .

Figure 4 displays the experimental melting points of PPS/DPA gels, measured by DSC, and the best-fit melting point

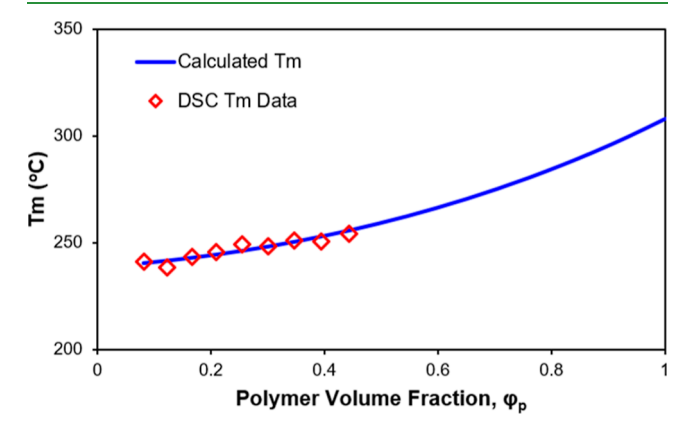


Figure 4. PPS/DPA melting point versus polymer volume fraction. Open diamonds = experimental melting point via DSC. The solid line represents the calculated melting temperature profile using eq 5.

depression profile using eq 5. Over the polymer volume fraction range of 0.08-0.44 (10-50 wt % PPS), the experimental melting points show excellent agreement with Flory's melting point depression and the compositional dependence expected for a S–L phase separation process. From the fit, χ is calculated as 0.41, indicative of a relatively good solvent. This value agrees well with $\chi = 0.49$ calculated using HSPs and thus validates the HSPs for DPA calculated from group contributions. Comparatively, other PPS TIPS systems have observed S-L phase separation at higher values of χ , such as Fan et al.³⁹ with a 25/75 wt % mixture of diphenyl ketone and benzoin ($\chi = 1.48$). Therefore, since the value of $\chi = 0.41$ indicates that DPA is a good solvent for PPS, it is reasonable to conclude that the TIPS process with PPS/DPA mixtures follows the S-L phase behavior (Figure 2a). The combination of information from the phase diagram, HSP, and now the melting point depression all suggest that PPS-DPA has favorable interactions, which strongly supports the assignment of S-L phase separation. Identifying the phase separation mechanism is vital to designing aerogel processing conditions and interpreting morphologies observed via scattering and microscopic techniques.

Morphological Evaluation of PPS Aerogels. Many semicrystalline aerogels exhibit a hierarchical structure, which can be elucidated by X-ray scattering experiments. 16,59 Hierarchical morphologies present distinct scattering features across multiple length scales, revealed by composite scattering profiles from merged WAXS, SAXS, and USAXS data. These profiles reveal a complex order, from the organization of polymer chains in crystallographic unit cells to individual crystalline lamella comprised of many unit cells to much larger aggregates (stacks) of chain-folded lamella.

Figure 5a shows the merged USAXS, SAXS, and WAXS scattering profiles of three concentrations of PPS aerogels 10, 15, and 20 w/v %. These scattering profiles reveal multiple features and indicate that PPS aerogels contain a hierarchical

ACS Applied Polymer Materials

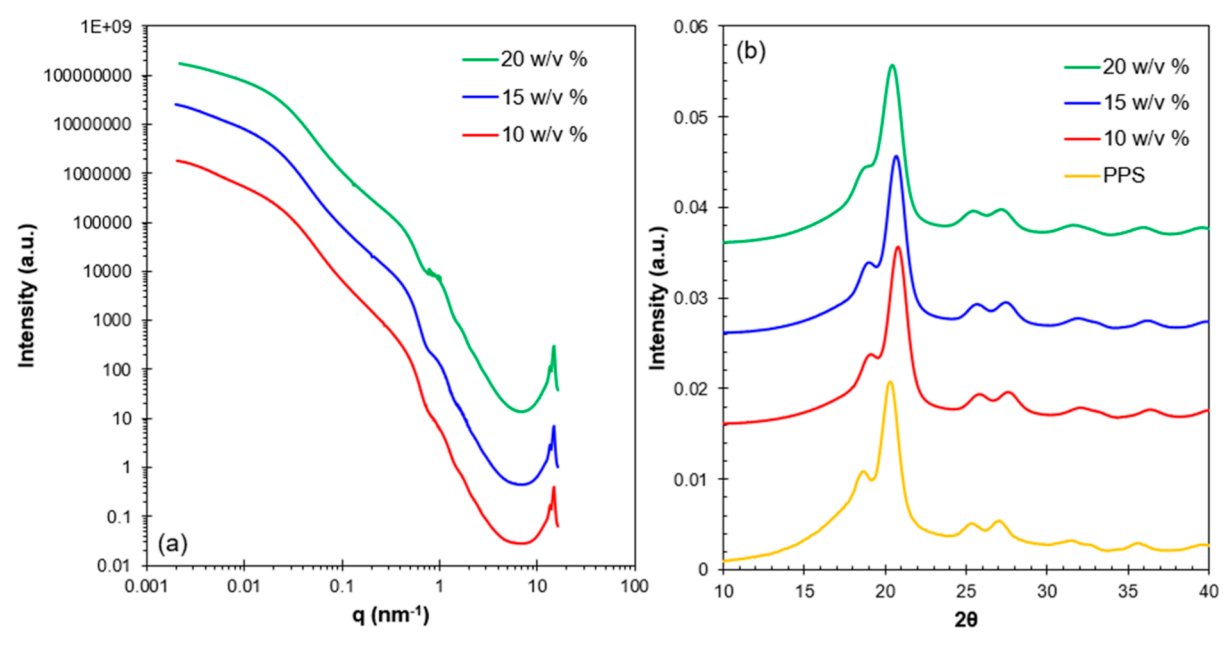


Figure 5. (a) USAXS/SAXS/WAXS scattering profiles of 10, 15, and 20 w/v % PPS aerogels. (b) WAXS scattering profiles of 10, 15, and 20 w/v % PPS aerogels and a bulk, semicrystalline PPS film (melt-pressed at 330 °C; cooled slowly to R.T.) for comparison. Scattering profiles have been shifted vertically for clarity.

morphology comprised of structure over a wide range of length scales. Scattering profiles for all aerogel compositions tested in this work (10–30 w/v %) display similar features and can be found in the Supporting Information (Figure S2). All three PPS aerogel profiles reveal similar key features—knees at q=0.02 nm⁻¹ and q=0.5 nm⁻¹, along with oscillations in the region 0.5 nm⁻¹ < q<3 nm⁻¹. At q=0.5 nm⁻¹, the observed knee is similar to a knee detected in semicrystalline PEEK/DCA aerogels (q=0.35 nm⁻¹), which has been attributed to scattering from the crystalline lamella. Based on the similarities between the scattering profiles of PEEK and PPS, the knee at q=0.5 nm⁻¹ in Figure 5a is attributed to the PPS crystalline lamella.

At scattering vectors larger than the knee at $q = 0.5 \text{ nm}^{-1}$ in Figure 5a, oscillations are observed in the scattering pattern. Similar oscillations were observed in PEEK/DCA and PEEK/4CP aerogels but with smaller amplitudes. In a randomly arranged platelet system, Beaucage and co-workers attributed oscillations in the regime $0.3 \text{ nm}^{-1} < q < 10 \text{ nm}^{-1}$ to a form factor arising from relatively monodisperse platelet thicknesses. As the feature at $q = 0.5 \text{ nm}^{-1}$ in the PPS aerogel is attributed to scattering of the crystalline lamella, the oscillations at $q > 0.5 \text{ nm}^{-1}$ suggest an ordered structure with rather uniform lamellar thicknesses in these PPS aerogels.

The scattering knee at $q=0.02~\mathrm{nm}^{-1}$ (Figure 5a) originates from the largest feature in the hierarchical structure. In our previous studies of hierarchical, semicrystalline PEEK/4CP and PEEK/DCA aerogels, the low q feature was attributed to the radius of gyration of globular lamellar stacks, as observed by SEM. Similarities between the PEEK and PPS aerogel scattering profiles suggest that the low q knee in these PPS/DPA aerogels can also be attributed to a characteristic dimension of PPS lamellar stacks. To estimate the global average dimensions of the observed scattering features, a fitting function must be applied to the scattering profile.

PPS aerogel scattering profiles were fit using the Unified Function, developed by Beaucage. ⁶⁰ Table 1 highlights fitting parameters from the Unified Fit of the PPS aerogel scattering

Table 1. Radius of Gyration, R_g , and Power-Law Slope, P, of PPS Aerogels

sample	$R_{g,2}$ (nm)	P_2	$R_{g,1}$ (nm)	P_1
PPS 10 w/v %	98.5	4.0	5.8	4.0
PPS 15 w/v %	110.1	4.0	5.1	4.0
PPS 20 w/v %	95.6	4.0	4.7	3.9

curves, where $R_{g,1}$ and P_1 represent the radius of gyration and power-law exponent of the knee located at about $q = 0.5 \text{ nm}^{-1}$, while $R_{g,2}$ and P_2 define those same respective quantities for the knee located at $q = 0.02 \text{ nm}^{-1}$. According to the Unified Fit, $R_{g,1}$ was found to be in the range of 4.7 to 5.8 nm for the PPS aerogels; these parameters are consistent with comparable values observed in PEEK aerogels 16 and justify the attribution of the high q knee to scattering from the PPS crystalline lamella. PPS R_{g,1} values were also found to decrease as polymer concentration increased. One possible explanation for this phenomenon is that the lamellar thickness decreases as the polymer concentration increases due to increasing entanglement density. This phenomenon of entanglements limiting lamellar thickness was observed by Luo et al.⁶¹ in molecular dynamics simulations of concentrated PVA chains in solution (volume fraction PVA: $\phi_{\rm P}$ = 0.525 to 1). Moreover, experimental investigations of the nucleation rate of polyethylene by Hikosaka et al.⁶² revealed that increased entanglement density suppresses chain diffusion to the crystal growth front and that this entanglement density displays an inverse relationship with lamellar thickness. With respect to the surface characteristics of the lamellar features, P_1 is equivalent to 4.0 for all three concentrations of PPS. Satisfying Porod's law, this indicates that the feature at $q = 0.5 \text{ nm}^{-1}$ has sharp, well-defined interfaces, typical for crystalline lamellae. 60,63

The fitting parameters of the low-q feature at q = 0.02 nm⁻¹ are also listed in Table 1. The $R_{\rm g,2}$ values were found to be in the range of 95 to 111 nm and show no clear correlation with polymer concentration. P_2 values are also constant at 4.0, indicating that the larger morphological features also display

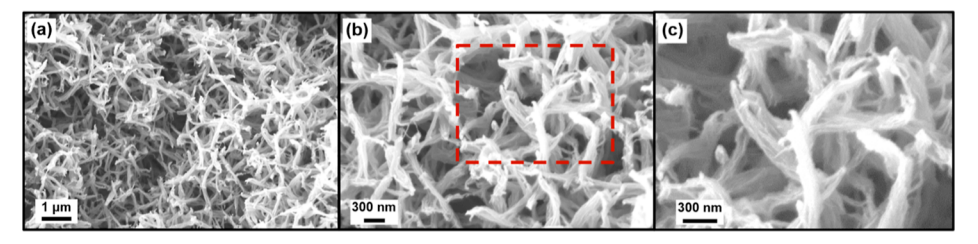


Figure 6. SEM micrographs of a 15 w/v % PPS aerogel. Magnifications: (a) = $25k \times$, (b) = $60k \times$, and (c) = $60k \times$ [zoomed-in area within the red box of (b)].

sharp interfaces. In comparison, the $R_{\rm g,2}$ values of PEEK/DCA and PEEK/4CP aerogels were found to similar to be those listed in Table 1, again suggesting that the origin of the low-q knee in PPS aerogels may be attributed to lamellar aggregates. Interestingly, the P_2 values for PPS aerogels were different than those for PEEK aerogels, suggesting differences in the lamellar aggregate surface textures. In the PPS aerogels, the P_2 values were all equal to 4, suggesting sharp, smooth interfaces of the lamellar aggregates. In contrast, the PEEK aerogels demonstrated P_2 values between 2.3 and 3.5, indicative of surface or mass fractals, 16 as confirmed by SEM.

Figure 5b compares the WAXS diffraction patterns of the PPS aerogels to those of bulk, semicrystalline PPS in the angular region from 10 to 40° 2θ . The bulk PPS sample shows crystalline reflections characteristic of the established body-centered orthorhombic unit cell for poly(p-phenylene sulfide). 64,65 By conventional integration of the Lorentz-corrected WAXS profile, the bulk PPS sample was determined to have a degree of crystallinity, $X_c = 22.6\%$ (Figure S3 and Table S4). The same characteristic reflections are observed for all of the aerogel samples, indicating that these PPS aerogels are semicrystalline with a crystal structure identical to bulk PPS. The degree of crystallinity values for the 10, 15, and 20 w/v % PPS aerogels were determined to be $X_c = 39.4\%$, $X_c = 36.3\%$, and $X_c = 38.4\%$, respectively, indicating relative consistency in the crystallinity of these aerogel specimens under the given gelation conditions. To confirm the consistency of the PPS crystal structure throughout the gelation process, a variable-temperature WAXS experiment with a 25 w/v % PPS/DPA gel was conducted. Figure S4 reveals that the PPS/DPA WAXS profile does not change upon dissolution at 270 °C and recrystallization.

While scattering provides average quantitative information about the hierarchical structure, direct microscopic imaging offers insights into local feature shapes, orientations, and textures. SEM micrographs of 15 w/v % PPS aerogels are displayed in Figure 6. SEM micrographs of all aerogel compositions (10-30 w/v %), which display nearly identical morphologies, can be found in Figure S5. The images reveal a fibrillar aerogel microstructure with features of relatively uniform size. The short, contorted fibrils appear branched and splayed at the ends and resemble axialites. These features appear to be isotropically oriented and homogeneously dispersed throughout the fibrillar network. Moreover, the axialites appear to be highly interconnected, forming a structurally stable network (see below). At higher magnifications in Figure 6b,c, individual layers can be observed within an axialite, which are attributed to individual lamellae that are stacked within the axialitic aggregates. Similar morphologies in thin PPS membranes, which were identified as bicontinuous microstructures, were also observed independently by Ding et al., ^{27,31} Fan et al., ³ Wang et al.,²⁸ and Zheng et al.³² using various single and bisolvent systems which all underwent L–L phase separation. Interestingly, in the PPS/DPA system, the axialites are a product of S–L phase separation, indicating that similar morphologies may form in PPS TIPS systems via multiple phase separation mechanisms.

Quantitative comparisons between the SEM micrographs and the USAXS Unified Fit parameters of the larger (low-q) morphological feature provide useful insight into the specific structural origin of the scattering feature. Based on ImageJ analysis of multiple 15 w/v % aerogel images, the average axialite is 1075 nm in length and 140 nm in width, displaying an approximate aspect ratio of 7.6. Table 1 indicates that the $R_{\rm g,2}$ of the 15 w/v % PPS aerogel equals 110.1 nm, and this dimension is comparable to the average axialite width (i.e., the average thickness of the fibrils). Since any scattering from a feature attributed to the axialite length (greater than 1 μ m) is outside of the measurable range of these USAXS data, the low-q Guinier knee centered at about $q=0.02~{\rm nm}^{-1}$ is thus attributed to the thickness of the fibrillar aggregates of stacked lamella based on reasonable agreement between microscopy and scattering.

In order to elucidate any effect of porosity on the low-q scattering of PPS aerogels, two additional experiments were performed. First, scattering data was collected on a 25 w/v % PPS/DPA solvated gel at 65 °C (above the melting point of DPA) and compared to a 25 w/v % PPS aerogel (Figure S6). While the low-q intensity of the solvent-free aerogel is higher than that of the solvated gel due to the high electron density contrast between the air-containing pores and polymer, the USAXS and SAXS knees are essentially unaffected by the porosity. The Unified fitting parameter for the low-q feature, $R_{\rm g,2}$, is practically identical between the two systems (aerogel $R_{\rm g,2}$ = 86.7 nm, PPS/DPA gel $R_{\rm g,2}$ = 83.1 nm), suggesting that the aerogel porosity does not significantly affect the dimension of this feature.

To further highlight the crystalline contribution to the aerogel scattering profiles, a contrast-matching experiment was also performed. Contrast matching is used in porous materials research 16,66 to manipulate the electron density contrast in a multiphase system in order to highlight scattering contributions from a certain phase. In PPS aerogels, there are three phases of varying electron density—air, PPS amorphous domains, and PPS crystalline domains. Removing air as a source of contrast by filling the aerogel pores with a material which has the same electron density as amorphous PPS accentuates scattering features originating from crystalline PPS. The scattering length densities (SLD) of amorphous and crystalline PPS were calculated to be 11.691 and 12.665 \times 10⁻⁶/Å² (calculations are detailed in the Supporting Information). To contrast-match amorphous PPS, a 20 w/v % PPS aerogel was submerged in mixtures of ethanol and Cyrene, a bio-renewable solvent which was found to have a comparable SLD to amorphous PPS

ACS Applied Polymer Materials

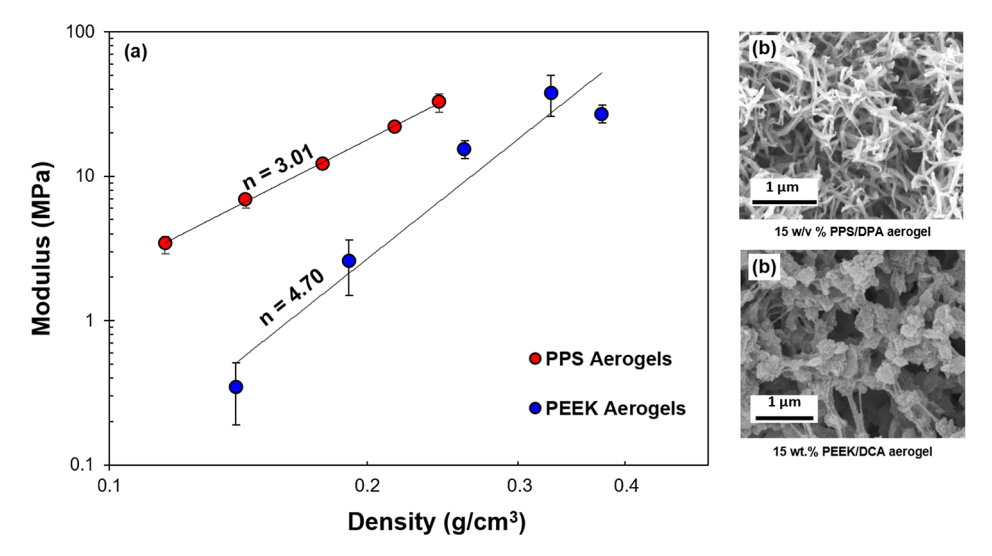


Figure 7. (a) Compressive modulus versus density plots for PPS and PEEK aerogels and (b) SEM micrographs of PPS/DPA aerogels and PEEK/DCA aerogels. Reproduced with permission from Talley, S. J.; Vivod, S. L.; Nguyen, B. A.; Meador, M. A. B.; Radulescu, A.; Moore, R. B. Hierarchical Morphology of Poly(ether ether ketone) Aerogels. ACS Applied Materials and Interfaces 2019, 11 (34), 31508–31519. DOI: 10.1021/acsami.9b09699. Copyright 2019 American Chemical Society.

 $(11.303 \times 10^{-6}/\text{Å}^2, 97\% \text{ match})$, for 96 h prior to performing the scattering experiments.

Merged USAXS/SAXS scattering profiles of dry and Cyrene/ethanol imbibed 20 w/v % PPS aerogels are shown in Figure S7. Dry and Cyrene-soaked aerogels generally display similar scattering features. The high-q scattering knee sharpens slightly in the presence of Cyrene, indicating that filling the aerogel nano-scale porosity with Cyrene helps to increase the resolution of this feature. The low-q knee, attributed to the lamellar aggregates, is virtually unchanged in the Cyrene-soaked gel, confirming that the feature is of crystalline origin and validating the assignment of this feature from both USAXS data and SEM micrographs to the PPS lamellar aggregates. A detailed understanding of PPS aerogel morphology provides context for the observed mechanical behavior.

Correlation between the Structure and Mechanical **Properties of PPS Aerogels.** To highlight the impact of morphology on mechanical properties, we draw comparisons to our recent work with PEEK aerogels, as both PPS and PEEK have comparable bulk moduli. Figure 7 shows the relationship between Young's modulus and density of PPS and PEEK¹⁶ aerogels under uniaxial compression. Tabulated values for PPS aerogel density, modulus, and volumetric porosity are reported in Table S1. Full compressive stress versus strain profiles are also found in the Supporting Information (Figure S8). As the aerogel density increases with increasing polymer concentration, the modulus also increases, which is typical of natural and synthetic porous bodies. 67-69 PPS aerogels demonstrate significantly higher moduli than PEEK aerogels over the given range of densities. This divergence in the modulus versus density behavior is especially obvious at low densities, where the 10 w/v % PPS aerogel displays a modulus approximately an order of magnitude greater than the lowest density PEEK aerogel. The two divergent modulus-versus-density trends suggest that load distribution in the physical networks of PPS and PEEK aerogels is dictated not solely by their bulk polymer properties (both PPS and PEEK display a Young modulus of approximately 3.6 GPa²⁵) but also by their specific morphologies.

Trends in the response of aerogels to uniaxial compression can give insights into the structure and deformation behavior of these polymeric networks. Gibson and Ashby⁶⁷ and Hilyard,⁷⁰ among others, found that a simple power-law relationship exists for relating the dependence of the normalized modulus on the normalized density for a porous structural material

$$\left(\frac{E}{E_{\rm s}}\right) \sim \left(\frac{\rho}{\rho_{\rm s}}\right)^n \tag{6}$$

where E and E_s represent the compressive moduli of the aerogel and bulk (subscript s—solid) material, ρ and ρ_s are the densities of the aerogel and bulk material, and n is the scaling exponent obtained from the slope of the normalized log modulus versus normalized log density. As n increases, so does the density dependence of the compressive modulus.

In porous solids, n is related to the mode of structural deformation under uniaxial compression. When n = 2, theory and experiment both indicate that load-bearing features form a cooperative network that deforms by bending and buckling in compression. At low densities, the network is well connected and distributes load efficiently; therefore, increasing density simply adds more support to an already robust framework. 67,69 The slopes, n, of PPS and PEEK aerogels equal 3.01 and 4.70, respectively (see Figure S9). Clearly, the PPS aerogels exhibit a much lower modulus-versus-density scaling factor, n, than that of PEEK. Thus, the PPS aerogels are much more efficient at distributing compressive loads, and their resistance to deformation may include contributions from bending and buckling of the fibrillar features. This behavior is attributed to the highly interconnected, fibrillar microstructure of the PPS aerogels compared to the globular microstructure of the PEEK aerogels.

In contrast, PEEK aerogels display a power-law scaling value of n=4.70, which is significantly larger than the power-law exponent observed in silica mass fractal structures (n=3.6). Physically, this indicates that the modulus of PEEK aerogels scales with density to a much greater extent, likely because there are no bending members to transmit load efficiently throughout the structure. As density within these fractal-like structures increases, more spherical particles are added to a given volume; this will greatly increase the aerogel modulus since the mass

fractal features are much more incompressible than void space. SEM micrographs in Figure 7b highlight the morphological differences between PPS aerogels, comprised of interconnected axialites, and PEEK aerogels, comprised of a mass fractal system made up of globular features. Thus, the scaling law determined via mechanical testing is consistent with the morphologies observed by microscopy.

CONCLUSIONS

A process for creating poly(phenylene sulfide) gels and aerogels at various compositions using a benign solvent, 1,3-diphenylacetone, has been presented. The phase diagram for the PPS/ DPA system is consistent with solid-liquid phase separation, where the resulting aerogel morphology is controlled by PPS crystallization within the solvent. Calculation of the Flory-Huggins interaction parameter through melting point depression ($\chi = 0.41$) and the HSP approach ($\chi = 0.49$) both confirm favorable polymer-solvent interactions, as is characteristic for the S-L phase separation mechanism. X-ray scattering and SEM reveal the hierarchical, interconnected fibrillar morphology of PPS aerogels. In comparison to PEEK aerogels formed by the TIPS process, the microstructural differences between PEEK aerogels (globular aggregates) and PPS aerogels (fibrillar aggregates) have a significant effect on the observed mechanical behavior. Scaling relationships between compressive modulus and aerogel density suggest that fibrillar structural elements of PPS aerogels are more efficient at distributing compressive loads relative to the mass-fractal, globular structural elements of PEEK aerogels. This work sets the stage for further fundamental investigations into the process-structure-property relationships of polymeric aerogels and their application as mechanically robust, lightweight structural elements..

ASSOCIATED CONTENT

Supporting Information

The Supporting Information is available free of charge at https://pubs.acs.org/doi/10.1021/acsapm.3c01171.

Brightness versus temperature cloud point data; PPS aerogel concentration, density, porosity, and compressive modulus; calculations of the HSP of DPA and BBP; USAXS/SAXS scattering of all aerogel compositions; WAXS deconvolutions and percent crystallinity of PPS aerogels and melt-crystallized film; variable-temperature WAXS of 25 w/v % PPS/DPA gel; SEM micrographs of all aerogel compositions; USAXS/SAXS scattering profiles of 25 w/v % aerogel and solvated gel; scattering length density formula; USAXS/SAXS scattering profiles of 20 w/v % aerogel and contrast-matched gel; compressive stress versus strain data for all aerogel compositions; and normalized modulus versus density plot of PPS and PEEK aerogels (PDF)

AUTHOR INFORMATION

Corresponding Author

Robert B. Moore — Department of Chemistry, Macromolecules Innovation Institute, Virginia Tech, Blacksburg, Virginia 24061, United States; oorcid.org/0000-0001-9057-7695; Email: rbmoore3@vt.edu

Authors

Garrett F. Godshall – Department of Chemistry, Macromolecules Innovation Institute, Virginia Tech, Blacksburg, Virginia 24061, United States; oorcid.org/0000-0002-8360-4605

Glenn A. Spiering — Department of Chemistry, Macromolecules Innovation Institute, Virginia Tech, Blacksburg, Virginia 24061, United States; orcid.org/0000-0002-4758-9276

Erin R. Crater — Department of Chemistry, Macromolecules Innovation Institute, Virginia Tech, Blacksburg, Virginia 24061, United States; orcid.org/0000-0001-5334-469X

Complete contact information is available at: https://pubs.acs.org/10.1021/acsapm.3c01171

Author Contributions

The manuscript was written through the contributions of all authors. All authors have given approval to the final version of the manuscript.

Notes

The authors declare no competing financial interest.

ACKNOWLEDGMENTS

This material is based upon work supported by the National Science Foundation under grant nos. DMR 2104856 and DMR 2018258. This research used the resources of the Advanced Photon Source, a U.S. Department of Energy (DOE) Office of Science user facility operated for the DOE Office of Science by Argonne National Laboratory under contract no. DE-AC02-06CH11357. USAXS/WAXS/WAXD data were collected on the 9-ID-C beamline at the APS, Argonne National Laboratory. This work used shared facilities at the Nanoscale Characterization and Fabribcation Laboratory, which is funded and managed by Virginia Tech's Institute for Critical Technology and Applied Science. Additional support is provided bythe Virginia Tech National Center for Earth and Environmental Nanotechnology Infrastrusture (NanoEarth), a member of the National Nanotechnology Coordinated Infrastructure (NNCI), supported ny NSF (ECCS 1542100 and ECCS 2025151).

REFERENCES

ī

- (1) Kistler, S. S. Coherent Expanded Aerogels and Jellies. *Nature* 1931, 127, 741.
- (2) Gupta, P.; Singh, B.; Agrawal, A. K.; Maji, P. K. Low density and high strength nanofibrillated cellulose aerogel for thermal insulation application. *Mater. Des.* **2018**, *158*, 224–236.
- (3) Idumah, C. I.; Ezika, A. C.; Okpechi, V. U. Emerging trends in polymer aerogel nanoarchitectures, surfaces, interfaces and applications. *Surf. Interfaces* **2021**, *25*, 101258.
- (4) Flory, P. J. Introductory Lecture. *Faraday Discuss. Chem. Soc.* **1974**, 57, 7–18.
- (5) Wang, L.; Pingitore, A. T.; Xie, W.; Yang, Z.; Perry, M. L.; Benicewicz, B. C. Sulfonated PBI Gel Membranes for Redox Flow Batteries. *J. Electrochem. Soc.* **2019**, *166*, A1449—A1455.
- (6) Hu, X.; Vatankhah-Varnoosfaderani, M.; Zhou, J.; Li, Q.; Sheiko, S. S. Weak Hydrogen Bonding Enables Hard, Strong, Tough, and Elastic Hydrogels. *Adv. Mater.* **2015**, *27*, 6899–6905.
- (7) Daniel, C.; Alfano, D.; Venditto, V.; Cardea, S.; Reverchon, E.; Larobina, D.; Mensitieri, G.; Guerra, G. Aerogels with a Microporous Crystalline Host Phase. *Adv. Mater.* **2005**, *17*, 1515–1518.
- (8) Daniel, C.; Dammer, C.; Guenet, J.-M. On the definition of thermoreversible gels: the case of syndiotactic polystyrene. *Polymer* **1994**, 35, 4243–4246.
- (9) Daniel, C.; Giudice, S.; Guerra, G. Syndiotatic Polystyrene Aerogels with β , γ , and ε Crystalline Phases. *Chem. Mater.* **2009**, 21, 1028–1034
- (10) Hong, H.; Pan, Y.; Sun, H.; Zhu, Z.; Ma, C.; Wang, B.; Liang, W.; Yang, B.; Li, A. Superwetting polypropylene aerogel supported form-stable phase change materials with extremely high organics loading and

- enhanced thermal conductivity. Sol. Energy Mater. Sol. Cells 2018, 174, 307–313.
- (11) Daniel, C.; Longo, S.; Cardea, S.; Vitillo, J. G.; Guerra, G. Monolithic nanoporous—crystalline aerogels based on PPO. *RSC Adv.* **2012**, *2*, 12011–12018.
- (12) Chen, X.; Liang, Y. N.; Tang, X.-Z.; Shen, W.; Hu, X. Additive-free poly (vinylidene fluoride) aerogel for oil/water separation and rapid oil absorption. *Chem. Eng. J.* **2017**, 308, 18–26.
- (13) Praveena, N. M.; Virat, G.; Krishnan, V. G.; Gowd, E. B. Stereocomplex formation and hierarchical structural changes during heating of supramolecular gels obtained by polylactide racemic blends. *Polymer* **2022**, *241*, 124530.
- (14) Krishnan, V. G.; Praveena, N. M.; Raj, R. B. A.; Mohan, K.; Gowd, E. B. Thermoreversible Gels of Poly(l-lactide)/Poly(d-lactide) Blends: A Facile Route to Prepare Blend α -Form and Stereocomplex Aerogels. *ACS Appl. Polym. Mater.* **2023**, *5*, 1556–1564.
- (15) Talley, S. J.; Yuan, X.; Moore, R. B. Thermoreversible Gelation of Poly(ether ether ketone). *ACS Macro Lett.* **2017**, *6*, 262–266.
- (16) Talley, S. J.; Vivod, S. L.; Nguyen, B. A.; Meador, M. A. B.; Radulescu, A.; Moore, R. B. Hierarchical Morphology of Poly(ether ether ketone) Aerogels. *ACS Appl. Mater. Interfaces* **2019**, *11*, 31508–31519.
- (17) Talley, S. J.; AndersonSchoepe, C. L.; Berger, C. J.; Leary, K. A.; Snyder, S. A.; Moore, R. B. Mechanically robust and superhydrophobic aerogels of poly(ether ether ketone). *Polymer* **2017**, *126*, 437–445.
- (18) Kim, S. J.; Raut, P.; Jana, S. C.; Chase, G. Electrostatically Active Polymer Hybrid Aerogels for Airborne Nanoparticle Filtration. ACS Appl. Mater. Interfaces 2017, 9, 6401–6410.
- (19) Hees, T.; Zhong, F.; Rudolph, T.; Walther, A.; Mülhaupt, R. Nanocellulose Aerogels for Supporting Iron Catalysts and In Situ Formation of Polyethylene Nanocomposites. *Adv. Funct. Mater.* **2017**, 27, 1605586.
- (20) Leroy, A.; Bhatia, B.; Kelsall, C. C.; Castillejo-Cuberos, A.; Di Capua H, M.; Zhao, L.; Zhang, L.; Guzman, A. M.; Wang, E. N. Highperformance subambient radiative cooling enabled by optically selective and thermally insulating polyethylene aerogel. *Sci. Adv.* **2019**, *5*, 1–8.
- (21) Anderson, L. J.; Moore, R. B. Sulfonation of blocky brominated PEEK to prepare hydrophilic-hydrophobic blocky copolymers for efficient proton conduction. *Solid State Ionics* **2019**, *336*, 47–56.
- (22) Noble, K. F.; Troya, D.; Talley, S. J.; Ilavsky, J.; Moore, R. B. High-Resolution Comonomer Sequencing of Blocky Brominated Syndiotactic Polystyrene Copolymers Using 13C NMR Spectroscopy and Computer Simulations. *Macromolecules* **2020**, *53*, 9539–9552.
- (23) Kasprzak, C. R.; Anderson, L. J.; Moore, R. B. Tailored sequencing of highly brominated Poly(ether ether ketone) as a means to preserve crystallizability and enhance Tg. *Polymer* **2022**, *251*, 124918.
- (24) Zuo, P.; Tcharkhtchi, A.; Shirinbayan, M.; Fitoussi, J.; Bakir, F. Overall Investigation of Poly (Phenylene Sulfide) from Synthesis and Process to Applications A Review. *Macromol. Mater. Eng.* **2019**, 304, 1800686.
- (25) Brostow, W. Mechanical Properties. In *Physical Properties of Polymers Handbook*; Mark, J. E., Ed.; Springer New York, 2007; pp 423–445.
- (26) Rahate, A. S.; Nemade, K. R.; Waghuley, S. A. Polyphenylene sulfide (PPS): state of the art and applications. *Rev. Chem. Eng.* **2013**, 29, 471–489.
- (27) Ding, H.; Zhang, Q.; Tian, Y.; Shi, Y.; Liu, B. Preparation of porous structure in the system of PEEK/PPS/diphenyl ketone via thermally induced phase separation. *J. Appl. Polym. Sci.* **2007**, *104*, 1523–1530.
- (28) Wang, X.; Li, Z.; Zhang, M.; Fan, T.; Cheng, B. Preparation of a polyphenylene sulfide membrane from a ternary polymer/solvent/non-solvent system by thermally induced phase separation. *RSC Adv.* **2017**, 7, 10503—10516.
- (29) Han, X.; Ding, H.; Wang, L.; Xiao, C. Effects of nucleating agents on the porous structure of polyphenylene sulfide via thermally induced phase separation. *J. Appl. Polym. Sci.* **2008**, 107, 2475—2479.

- (30) Fan, T.; Miao, J.; Li, Z.; Cheng, B. Bio-inspired robust superhydrophobic-superoleophilic polyphenylene sulfide membrane for efficient oil/water separation under highly acidic or alkaline conditions. *J. Hazard. Mater.* **2019**, 373, 11–22.
- (31) Ding, H.; Zeng, Y.; Meng, X.; Tian, Y.; Shi, Y.; Jiao, Q.; Zhang, S. Porous polyphenylene sulfide membrane with high durability against solvents by the thermally induced phase-separation method. *J. Appl. Polym. Sci.* **2006**, *102*, 2959–2966.
- (32) Zheng, H.; Zhu, S.; Yu, W.; Zhou, C. Comparison of Various Solvents for Poly(Phenylene Sulfide) Microporous Membrane Preparation via Thermally Induced Phase Separation. *J. Macromol. Sci., Part B: Phys.* **2014**, 53, 1477–1496.
- (33) Daniel, C.; Longo, S.; Guerra, G. High porosity polyethylene aerogels. *Polyolefins J.* **2015**, *2*, 49–55.
- (34) Lermontov, S. A.; Malkova, A. N.; Sipyagina, N. A.; Straumal, E. A.; Maksimkin, A. V.; Kolesnikov, E. A.; Senatov, F. S. Properties of highly porous aerogels prepared from ultra-high molecular weight polyethylene. *Polymer* **2019**, *182*, 121824.
- (35) Wang, G.; Peng, L.; Yu, B.; Chen, S.; Ge, Z.; Uyama, H. Hierarchically porous sponge for oily water treatment: Facile fabrication by combination of particulate templates and thermally induced phase separation method. *J. Ind. Eng. Chem.* **2018**, *62*, 192–196.
- (36) Zou, L.; Phule, A. D.; Sun, Y.; Zhu, T. Y.; Wen, S.; Zhang, Z. X. Superhydrophobic and superoleophilic polyethylene aerogel coated natural rubber latex foam for oil-water separation application. *Polym. Test.* **2020**, *85*, 106451.
- (37) Lloyd, D. R.; Kim, S. S.; Kinzer, K. E. Microporous membrane formation via thermally-induced phase separation. II. Liquid-liquid phase separation. *J. Membr. Sci.* **1991**, *64*, 1–11.
- (38) Lloyd, D. R.; Kinzer, K. E.; Tseng, H. S. Microporous membrane formation via thermally induced phase separation. I. Solid-liquid phase separation. *J. Membr. Sci.* **1990**, *52*, 239–261.
- (39) Fan, T.; Li, Z.; Cheng, B.; Li, J. Preparation, characterization of PPS micro-porous membranes and their excellent performance in vacuum membrane distillation. *J. Membr. Sci.* **2018**, *556*, 107–117.
- (40) Synthetic Flavoring Substances and Adjuvants; Food and Drug Administration, 2018.
- (41) Hurd, C. D.; Thomas, C. L. Preparation of Dibenzyl Ketone and Phenylacetone. *J. Am. Chem. Soc.* **1936**, *58*, 1240.
- (42) Ilavsky, J.; Jemian, P. R.; Allen, A. J.; Zhang, F.; Levine, L. E.; Long, G. G. Ultra-small-angle X-ray scattering at the Advanced Photon Source. *J. Appl. Crystallogr.* **2009**, 42, 469–479.
- (43) Ilavsky, J.; Zhang, F.; Allen, A. J.; Levine, L. E.; Jemian, P. R.; Long, G. G. Ultra-Small-Angle X-ray Scattering Instrument at the Advanced Photon Source: History, Recent Development, and Current Status. *Metall. Mater. Trans. A* **2013**, *44*, 68–76.
- (44) Ilavsky, J. Nika: software for two-dimensional data reduction. *J. Appl. Crystallogr.* **2012**, 45, 324–328.
- (45) Ilavsky, J.; Jemian, P. R. Irena: tool suite for modeling and analysis of small-angle scattering. *J. Appl. Crystallogr.* **2009**, 42, 347–353
- (46) Vonk, C. G. Computerization of Ruland's X-ray Method for Determination of the Crystallinity in Polymers. *J. Appl. Crystallogr.* **1973**, *6*, 148–152.
- (47) Beck, H. N. Solubility characteristics of poly(etheretherketone) and poly(phenylene sulfide). *J. Appl. Polym. Sci.* **1992**, *45*, 1361–1366.
- (48) Kim, S. S.; Lloyd, D. R. Thermodynamics of polymer/diluent systems for thermally induced phase separation: 3. Liquid-liquid phase separation systems. *Polymer* **1992**, 33, 1047–1057.
- (49) Nishi, T.; Wang, T. T. Melting Point Depression and Kinetic Effects of Cooling on Crystallization in Poly(vinylidene fluoride)-Poly(methyl methacrylate) Mixtures. *Macromolecules* 1975, 8, 909–915
- (50) Güner, A.; Kibarer, G. The important role of thermodynamic interaction parameter in the determination of theta temperature, dextran/water system. *Eur. Polym. J.* **2001**, *37*, 619–622.
- (51) Hansen, C. M. Hansen Solubility Parameters: A User's Handbook; CRC Press, 2007.

- (52) Kim, J. F.; Jung, J. T.; Wang, H.; Drioli, E.; Lee, Y. M. 1.15 Effect of Solvents on Membrane Fabrication via Thermally Induced Phase Separation (TIPS): Thermodynamic and Kinetic Perspectives. *Comprehensive Membrane Science and Engineering*; Elsevier, 2017; pp 386–417.
- (53) Hansen, C. M. The Prigogine Corresponding States Theory, the χ_{12} Interaction Parameter, and the Hansen Solubility Parameters. Hansen Solubility Parameters: A User's Handbook; CRC Press, 2002; pp 25–42.
- (54) Stefanis, E.; Panayiotou, C. Prediction of Hansen Solubility Parameters with a New Group-Contribution Method. *Int. J. Thermophys.* **2008**, 29, 568–585.
- (55) Chiang, C.-Y.; Lloyd, D. R. Effects of Process Conditions on the Formation of Microporous Membranes via Solid-Liquid Thermally Induced Phase Separation. *J. Porous Mater.* **1996**, *2*, 273–285.
- (56) Flory, P. J. Thermodynamics of Crystallization in High Polymers. IV. A Theory of Crystalline States and Fusion in Polymers, Copolymers, and Their Mixtures with Diluents. *J. Chem. Phys.* **1949**, *17*, 223–240.
- (57) López, L. C.; Wilkes, G. L. Crystallization kinetics of poly(p-phenylene sulphide): effect of molecular weight. *Polymer* **1988**, 29, 106–113.
- (58) Wunderlich, B. Thermal Analysis of Polymeric Materials; Springer, 2005.
- (59) Beaucage, G.; Aubert, J. H.; Lagasse, R. R.; Schaefer, D. W.; Rieker, T. P.; Erlich, P.; Stein, R. S.; Kulkarni, S.; Whaley, P. D. Nano-Structured, Semicrystalline Polymer Foams. *J. Polym. Sci., Part B: Polym. Phys.* **1996**, *34*, 3063–3072.
- (60) Beaucage, G. Approximations Leading to a Unified Exponential/Power-Law Approach to Small-Angle Scattering. *J. Appl. Crystallogr.* **1995**, 28, 717–728.
- (61) Luo, C.; Kröger, M.; Sommer, J.-U. Entanglements and Crystallization of Concentrated Polymer Solutions: Molecular Dynamics Simulations. *Macromolecules* **2016**, *49*, 9017–9025.
- (62) Hikosaka, M.; Watanabe, K.; Okada, K.; Yamazaki, S. Topological Mechanism of Polymer Nucleation and Growth The Role of Chain Sliding Diffusion and Entanglement. *Interphases and Mesophases in Polymer Crystallization III*; Allegra, G., Ed.; Springer Berlin Heidelberg, 2005; pp 137–186.
- (63) Beaucage, G. Small-Angle Scattering from Polymeric Mass Fractals of Arbitrary Mass-Fractal Dimension. *J. Appl. Crystallogr.* **1996**, 29, 134–146.
- (64) Tabor, B. J.; Magré, E. P.; Boon, J. The crystal structure of poly-phenylene sulphide. *Eur. Polym. J.* **1971**, *7*, 1127–1133.
- (65) Napolitano, R.; Pirozzi, B.; Salvione, A. Crystal Structure of Poly(p-phenylene sulfide): A Refinement by X-ray Measurements and Molecular Mechanics Calculations. *Macromolecules* **1999**, 32, 7682–7687
- (66) Hua, D. W.; D'Souza, J. V.; Schmidt, P. W.; Smith, D. M. Pore Structure Analysis Via Small Angle X-Ray Scattering And Contrast Matching. *Studies in Surface Science and Catalysis*; Rouquerol, J., Rodríguez-Reinoso, F., Sing, K. S. W., Unger, K. K., Eds.; Vol. 87; Elsevier, 1994; pp 255–261.
- (67) Gibson, I. J.; Ashby, M. F. The mechanics of three-dimensional cellular materials. *Proc. R. Soc. London, Ser. A* **1982**, 382, 43–59.
- (68) Lemay, J. D. Mechanical Structure-Property Relationships of Microcellular, Low Density Foams. *Mater. Res. Soc. Symp. Proc.* **1990**, 207, 21–26.
- (69) Fan, H.; Hartshorn, C.; Buchheit, T.; Tallant, D.; Assink, R.; Simpson, R.; Kissel, D. J.; Lacks, D. J.; Torquato, S.; Brinker, C. J. Modulus—density scaling behaviour and framework architecture of nanoporous self-assembled silicas. *Nat. Mater.* **2007**, *6*, 418–423.
- (70) Hilyard, N. C. Mechanics of Cellular Plastics; Macmillan, 1982.